


Phonon-Induced Relocation of Valence Charge in Boron Nitride Observed by Ultrafast X-Ray Diffraction

Shekhar Priyadarshi¹,^{*} Isabel Gonzalez-Vallejo¹, Christoph Hauf,[†] Klaus Reimann¹,[‡] Michael Woerner,[§] and Thomas Elsaesser¹
Max-Born-Institut für Nichtlineare Optik und Kurzzeitspektroskopie, 12489 Berlin, Germany

 (Received 23 April 2021; revised 14 January 2022; accepted 14 February 2022; published 30 March 2022)

The impact of coherent phonon excitations on the valence charge distribution in cubic boron nitride is mapped by femtosecond x-ray powder diffraction. Zone-edge transverse acoustic (TA) two-phonon excitations generated by an impulsive Raman process induce a steplike increase of diffracted x-ray intensity. Charge density maps derived from transient diffraction patterns reveal a spatial transfer of valence charge from the interstitial region onto boron and nitrogen atoms. This transfer is modulated with a frequency of 250 GHz due to a coherent superposition of TA phonons related to the ^{10}B and ^{11}B isotopes. Nuclear and electronic degrees of freedom couple through many-body Coulomb interactions.

DOI: [10.1103/PhysRevLett.128.136402](https://doi.org/10.1103/PhysRevLett.128.136402)

Vibrational excitations of a crystal lattice play a key role for its thermodynamic equilibrium properties and non-equilibrium processes such as sound propagation, energy transport, and dissipation of excess energy. Phonons, which represent quantized excitations of normal modes of the crystal, are frequently described in the adiabatic limit by introducing a harmonic or anharmonic vibrational potential surface. The shape of this potential surface is determined by the electronic charge distribution in the particular electronic state and the resulting interatomic interactions. The adiabatic approximation has been applied widely for calculating phonon dispersion relations [1] and for interpreting nonlinear phonon dynamics [2–6].

The adiabatic limit breaks down whenever phonons induce electronic motions such as charge transfer between lattice sites or charge rearrangements in polar covalent bonds. Such phenomena occur in a wide range of materials including polar semiconductors and ferroelectrics. The classical core-shell model introduced by Cochran [7–9] treats this scenario by solving the mechanical equations of motion of coupled ions with polarizable electron clouds. The coupled nuclear and electronic motions account for basic dielectric properties of ferroelectrics and, in particular, allow for including local-field effects according to the Clausius-Mossotti relation [10].

Another manifestation of coupled nuclear-electronic motions is nonlinearities in the response of phonons to electromagnetic fields. In apolar semiconductors such as Si and Ge, one-phonon infrared absorption bands are absent for symmetry reasons, but absorption due to the simultaneous excitation of two phonons exists. Series of multiphonon absorption bands have also been observed in polar semiconductors such as InSb [11]. Their occurrence has been attributed to a phonon-induced deformation of the

charge distribution [12,13]. In a similar way, second- and higher-order Raman excitations of phonons require an electronic polarizability depending on products of different phonon coordinates [14].

Femtosecond x-ray powder diffraction experiments have generated transient electron density maps of polar crystalline materials, reflecting the impact of coherent low-frequency lattice motions on charge density. Upon dispersive excitation of coherent phonons in an electronically excited state, electronic charge is shifted on the length scale of interatomic distances, while the atomic displacements from their equilibrium positions are orders of magnitude smaller [15–17]. Qualitatively, this behavior is in line with the core-shell model. However, an in-depth analysis is hampered by the limited knowledge on the excited-state electronic structure and by the potential impact of concomitant electronic excitations. Thus, experimental insight in phonon-induced charge density changes in the electronic ground state is important and much better accessible for theoretical analysis. Moreover, electron relocations induced by thermally excited, in particular acoustic phonons in the ground state, affect the intensities of Bragg diffraction peaks directly and may lead to a behavior different from the Debye-Waller picture [18] in the independent-atom model.

In this Letter, we demonstrate the direct impact of nonequilibrium acoustic phonon excitations on the valence charge distribution in the electronic ground state of crystalline matter. Cubic boron nitride (*c*-BN) with the zincblende crystal structure [Fig. 1(a)] is chosen as a prototypical system, in which the small number of core electrons allows for mapping relocations of valence electrons by time-resolved x-ray diffraction. Transverse acoustic (TA) phonons, impulsively excited at the zone edge close to the *L* point by a second-order Raman process,

induce a pronounced transfer of valence charge from the interstitial regions onto the B and N atoms, connected with an increase of diffracted intensity, opposite to a Debye-Waller scenario. This nonadiabatic behavior is caused by the coupling of nuclear and electronic degrees of freedom via local electric fields.

The *c*-BN powder sample (supplier PlasmaChem) consists of crystallites with diameters of 165 ± 50 nm. The small crystallite size was chosen to avoid multiple x-ray scattering events within an individual crystallite, i.e., the x-ray diffraction experiment is in the kinematic diffraction limit [18]. To eliminate artifacts from laser-induced damage in the sample, a fresh sample was prepared every day by tightly pressing the powder into ≈ 100 μm thick pellets. All measurements were done at ambient temperature (300 K).

The experiments are based on a femtosecond time-resolved optical-pump-hard-x-ray-probe scheme. Sub-100-fs optical pulses centered at 800 nm ($E = 1.55$ eV) or 400 nm ($E = 3.1$ eV), i.e., far below the indirect band gap of *c*-BN at $E_g = 6.36$ eV [19], generate a coherent superposition of phonon states by impulsive second-order Raman scattering within the spectral envelope of the pulses. The impact of this lattice excitation on the electronic charge distribution is mapped by recording transient powder diffraction patterns from the excited sample with 100-fs hard-x-ray probe pulses. The differential transient charge density is then derived from the transient and equilibrium diffraction patterns.

Synchronized optical pump and hard-x-ray probe pulses are derived from a Ti:sapphire laser system, providing sub-50-fs pulses of an energy up to 5.2 mJ at a 1 kHz repetition rate (center wavelength 800 nm). From the pump pulse energies of 0.75 mJ at 800 nm and 0.18 mJ at 400 nm and the 500- μm pump spot size on the sample, one calculates peak intensities of 7.6 TW/cm² and 1.8 TW/cm², for which electronic interband excitations and displacively excited phonons are absent. The pump bandwidth of $\Delta E_p = 50$ meV (FWHM) allows for impulsive excitation of TA phonons at the *L* zone edge, while TA phonons at the *X* edge and optical phonons at $q = 0$ are beyond ΔE_p . Hard x-ray probe pulses at a photon energy of 8.04 keV (Cu K_α) are generated by focusing 4-mJ, 800-nm pulses onto a moving copper tape target (thickness 10 μm). The x-ray pulses emitted in transmission through the target have a duration of some 100 fs and are collected, monochromatized, and focused to a 100 μm spot size on the sample by a Montel multilayer mirror (Incoatec) [20–22]. The resulting x-ray flux is 5×10^6 photons/s. The x-ray photons diffracted from the sample are recorded by a large-area detector (Pilatus Dectris 1M), which provides the intensities of multiple Debye-Scherrer rings simultaneously. Integration over all pixels with identical scattering angle 2θ yields the x-ray intensity I as a function of 2θ showing the (111) and (200) reflections [Fig. 1(d)].

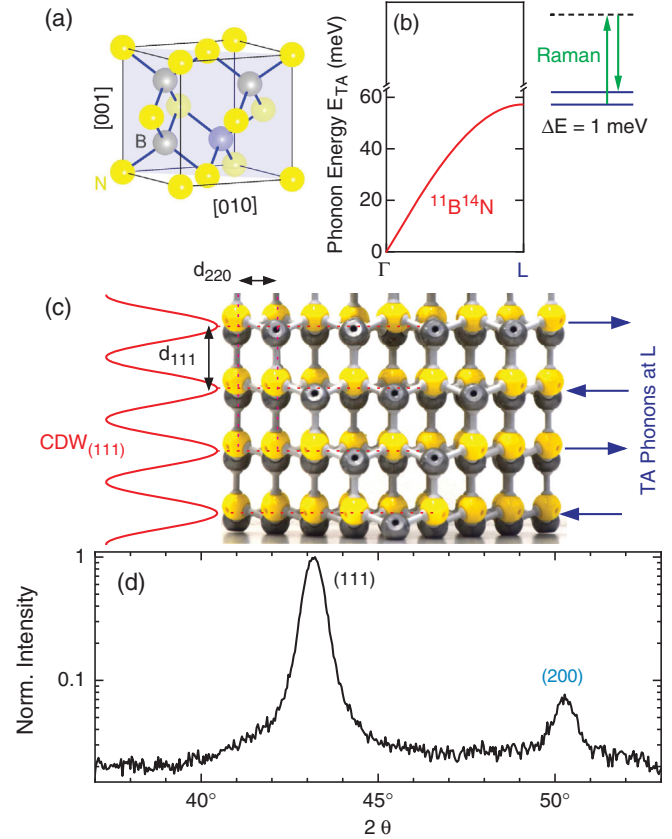


FIG. 1. (a) Unit cell of cubic boron nitride (*c*-BN) with the $(1\bar{1}0)$ plane shown in light blue. (b) Transverse acoustic (TA) phonon dispersion along the Γ -*L* direction in k space for isotopically pure $^{11}\text{B}^{14}\text{N}$. The arrows show schematically the Raman transitions. (c) Structure of *c*-BN viewed along the $[\bar{1}\bar{1}2]$ direction. The charge-density wave (red curve) determining the amplitude of the (111) Bragg reflection gains in intensity for a charge transfer from the interstitial regions onto the atoms. Blue arrows: atomic displacements of TA phonons at the *L* point. (d) Stationary diffraction intensity of *c*-BN powder, integrated over the Debye-Scherrer rings, measured with femtosecond x-ray pulses as a function of 2θ .

Data for each excitation wavelength were recorded for some 8000 pump-probe delay times in random order over approximately 50 experiment days. The x-ray intensity diffracted from the pumped and unpumped sample for each delay time t was measured alternately at a chopping rate of 25 Hz. The differential change in x-ray intensity is given by $\Delta I(t, \theta)/I_0(\theta) = [I_{\text{pumped}}(t, \theta) - I_{\text{unpumped}}(\theta)]/I_{\text{unpumped}}(\theta)$ [23]. The statistical uncertainty of $\Delta I/I_0$ is only 20 percent larger than expected for the shot-noise limit [21], allowing for the detection of very small transient x-ray intensity changes of $\Delta I/I_0 < 10^{-3}$.

Upon excitation by the optical pump pulse, one observes changes of diffracted intensity on both (111) and (200) reflections. In Figs. 2(a) and 2(b), intensity changes on the (111) reflection are plotted as a function of pump-probe delay for the two excitation wavelengths of 800 and

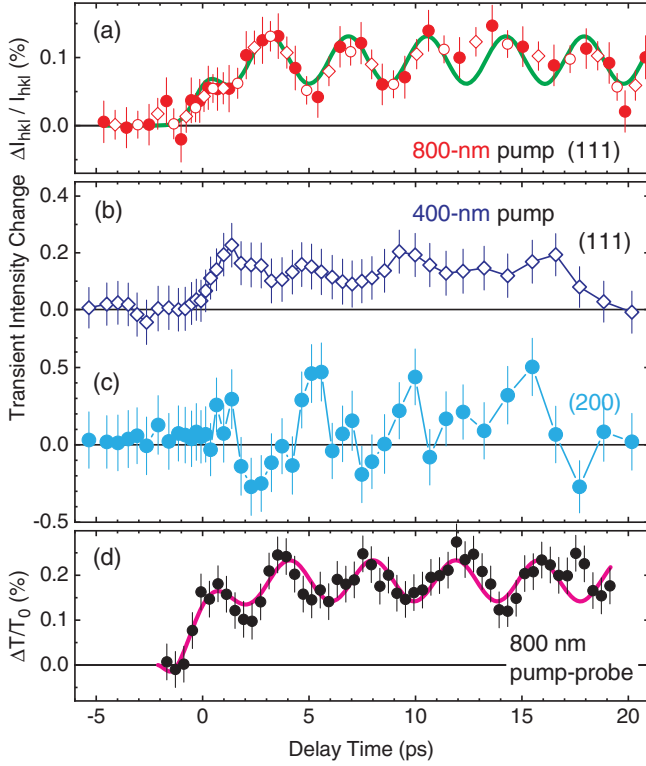


FIG. 2. (a) Transient intensity change $\Delta I_{hkl}/I_{hkl}$ of the (111) reflection after impulsive Raman excitation with femtosecond 800-nm pulses (solid circles, 1 ps temporal binning). Open symbols: same data with shifted 1-ps binning. Green line: steplike fit superimposed on oscillations with a frequency of 250 GHz. (b) Diamonds: same as in (a), but for excitation with 400-nm pulses. (c) Transient intensity change of the (200) reflection. (d) Time-resolved transmission change $\Delta T/T_0 = (T - T_0)/T_0$ of a *c*-BN crystallite as observed in an all-optical pump-probe experiment with femtosecond 800-nm pulses.

400 nm. One observes a steplike increase of diffracted intensity superimposed by oscillations. In spite of their small amplitudes of $\Delta I/I_0 < 10^{-3}$, the oscillations with a period of 4 ps can be followed for some 20 ps, underlining the very high experimental sensitivity. On the (200) reflection [Fig. 2(c)] for excitation with 400 nm, the oscillations display the same period with a larger amplitude, dominating over the steplike signal.

In additional femtosecond experiments, an 800 nm pump pulse induces coherent lattice motions in an individual larger *c*-BN crystallite via impulsive stimulated Raman scattering [24,25] and the resulting transmission change of the sample is recorded with an 800-nm probe pulse [23]. The time-resolved transmission change [Fig. 2(d)] exhibits oscillations with the same frequency as the x-ray transients.

Transient differential charge-density maps $\Delta\rho(\mathbf{r}, t) = \rho(\mathbf{r}, t) - \rho_0(\mathbf{r})$ are derived from the changes of diffracted x-ray intensity $\Delta I/I_0$ by analyzing the underlying changes of the x-ray structure factors with the maximum entropy method adapted to the conditions of the femtosecond

experiment [16,17,23,26–28]. Here, $\rho(\mathbf{r}, t)$ represents the electron density in the excited crystallite at delay time t , while $\rho_0(\mathbf{r})$ is the equilibrium electron density. For the small intensity changes shown in Fig. 2, $\Delta\rho(\mathbf{r}, t)$ depends linearly on intensity changes of the (111) and (200) Bragg reflections. The intensity change of the (111) reflection is connected with the charge transfer between the atoms and the interstitial region, whereas the (200) reflection results from the difference of electron densities on B and N atoms. Since only valence electrons are influenced by phonon excitations, it is not necessary to consider higher-indexed reflections, which depend predominantly on the density of spatially more localized core electrons [23,27,29].

In Fig. 3(a) we show $\rho_0(\mathbf{r})$ in the $(1\bar{1}0)$ plane of the unit cell [Fig. 1(a)], with local maxima of $\rho_0(\mathbf{r})$ on the B and N atoms. As a consequence of the limited spatial resolution, the charge density on the atoms and in the bond region between the atoms is not fully separated. There is a low quasicontinuous charge density throughout the $(1\bar{1}0)$ plane, in line with high-resolution charge density maps [30] and theoretical results [31]. In Figs. 3(b) and 3(c), $\Delta\rho(\mathbf{r}, t)$ induced by 400-nm excitation is shown for delay times of $t = 2.28$ ps and 5.46 ps. At $t = 2.28$ ps, charge

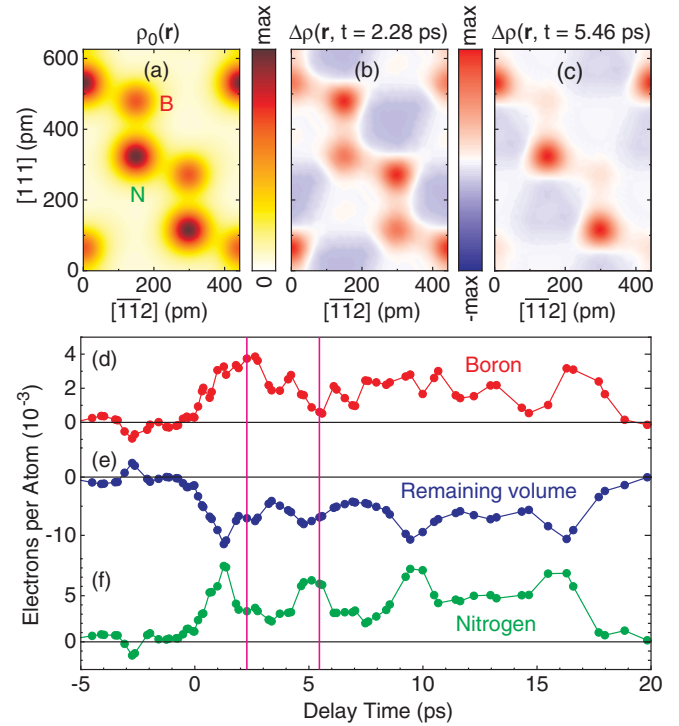


FIG. 3. (a) Stationary electron density $\rho_0(\mathbf{r})$ of *c*-BN in the $(1\bar{1}0)$ plane [linear scale, maximum $5340 \text{ e}^-/\text{nm}^3$]. (b), (c) Transient differential charge-density maps $\Delta\rho(\mathbf{r}, t)$ measured at delay times of $t = 2.28$ ps (b) and $t = 5.46$ ps (c) after 400 nm excitation. The scale in (b) and (c) is $\pm 6 \text{ e}^-/\text{nm}^3$. (d)–(f) Spatially integrated charge on the B and N atoms and in the remaining volume as a function of delay time. The vertical lines show the delay times for (b) and (c).

density is transferred from the interatomic regions of the unit cell almost equally to both boron (B) and nitrogen (N) atoms, reducing the difference in charge density on such two atoms and, thus, the intensity of the (200) reflection [Fig. 2(c)]. At $t = 5.46$ ps charge transfer towards the N atoms prevails, resulting in a maximum of (200) intensity. To illustrate charge dynamics within the c -BN unit cell, we integrated the differential electronic charge over spherical volumes around the B and N atoms and in the remaining volume of the unit cell. The transients in Figs. 3(d)–3(f) demonstrate an accumulation of charge on the atoms and a depletion in the rest of the unit cell. On top of a steplike kinetics, the charge density displays oscillatory components with opposite signs on the atoms and in the remaining volume.

We first discuss the phonon excitation process and the origin of the changes of diffracted intensity. In the electronic ground state of c -BN, impulsive Raman scattering within the bandwidth ΔE_p of the pump pulses generates a superposition of phonon quantum states. For $\Delta E_p = 50$ meV, excitation of an optical phonon with energies higher than 130 meV [31] is absent. However, TA phonons along the Γ - L direction in k space, which cover an energy range up to $E_{TA} = 56$ meV at the L point [Fig. 1(b)], are accessible via a second-order Raman process [32] within ΔE_p . While this excitation scheme covers the full Brillouin zone, TA phonons are predominantly generated close to the L point because of the very high density of phonon states there. The relevant excitation scheme is depicted in Fig. 1(b). It starts from thermally excited TA states at the L edge [33]. Figure 1(c) illustrates the related atomic displacements. A similar excitation of X-edge TA phonons is negligible because of limited ΔE_p , smaller thermal occupation and much smaller electronic polarizability [9].

The coupling of TA phonon excitations of the polar lattice and electronic degrees of freedom results in a change of valence charge density, by which the electrostatic energy in the unit cell is minimized. The deformation of charge density by nuclear motion has been a subject of early theoretical work, representing both nuclear and electronic degrees of freedom in the phonon [7–9,12]. The local-field and umklapp corrections in the microscopic electronic susceptibility of a crystal are essential for the coupling between nuclear and electronic degrees of freedom, which are most pronounced at the L point of the Brillouin zone (see also Fig. 2 of [9]).

The change in valence charge density gives rise to a change of x-ray structure factors governing the intensity of Bragg peaks. Both the steplike and oscillatory x-ray intensity changes observed in our experiments reflect the phonon-induced change of charge distribution, which is schematically illustrated for the (111) Bragg peak in Fig. 1(c). The oscillatory intensity changes are due to a quantum-coherent superposition of TA phonon states of different energies E_{TA} . The observed frequency of

250 GHz corresponds to an energy difference $\Delta E_{TA} = 1$ meV. The c -BN studied here contains the two stable isotopes of boron, ^{11}B and ^{10}B , in the natural ratio of 4:1 [34]. Acoustic phonons in isotopically pure $^{10}\text{B}^{14}\text{N}$ have a $\sqrt{25/24} - 1 \approx 2\%$ higher frequency than those in isotopically pure $^{11}\text{B}^{14}\text{N}$. This results, for TA phonons at the L point, in an energy difference of 1.2 meV, which matches the experimental ΔE_{TA} . We thus assign the oscillatory signals to a coherent superposition of isotopically separated TA phonon states, see also [[23], Sec. V] and [35–37].

This picture is independently supported by the impulsive stimulated Raman data [Fig. 2(d)], which display coherent oscillations with the same frequency, due to the coherent superposition of zone-edge TA phonon states. The weak damping of the oscillations on a time scale of tens of picoseconds points to a comparably long decoherence of this coherent superposition, requiring a long lifetime, but not a long decoherence time, of the TA phonons.

The intensity increase on the (111) and (200) diffraction peaks upon phonon excitation is in clear contrast to a Debye-Waller scenario. In the latter, the change of atomic positions connected with a phonon excitation results in a spatial smearing of electronic charge in the unit cell and a concomitant *decrease* of diffracted x-ray intensity. The intensity *increase* observed here requires a less broad distribution of valence electron density, which is accomplished by a charge transfer from the interatomic bond and other regions of the unit cell onto the B and N atoms.

For the small amounts of charge shifted upon TA phonon excitation [cf. Figs. 3(d)–3(f)], the modified valence structure of the crystal can be described by perturbation theory, i.e., by admixing wave functions of higher bands. In an elementary description of charge shift, we consider the microscopic interband current density $\mathbf{j}(\mathbf{r}) = \rho(\mathbf{r}) \cdot \mathbf{v}(\mathbf{r})$ [$\mathbf{v}(\mathbf{r})$: electron velocity] calculated with the coherent superposition $\cos(\eta)|\psi_{\text{HH,LH}}\rangle + \sin(\eta)\exp(i\phi)|\psi_{\text{CB}}\rangle$ of heavy-hole (HH) or light hole (LH) valence band states and a conduction band (CB) state. The wave functions are taken from pseudopotential calculations [38,39] for c -BN. The corresponding HH, LH, and CB charge densities in the (1 $\bar{1}$ 1) plane are shown in Fig. 4. The arrows show the irrotational charge-transfer contribution to the microscopic $\mathbf{j}(\mathbf{r})$ for a small admixture $\eta = 0.1$ and a phase ϕ corresponding to the maximum interband polarization current. The charge-transfer contribution to the strongest interband currents around the Γ point is spatially very localized and flows predominantly between the bond region and the atoms. The nuclear-displacement dipoles and the microscopic interband dipoles, i.e., the time integrals of interband currents, are localized at different positions in real space and couple via local electric fields as described by the Clausius-Mossotti relation [10]. Here, the zone edge at the L point plays a crucial role, because there hybrid phonon modes with nuclear and electronic degrees of freedom can form [7–9].

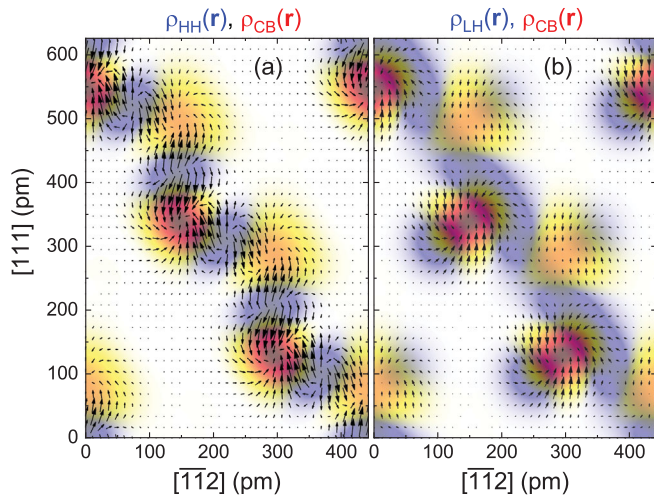


FIG. 4. Arrows: irrotational charge-transfer contribution to the microscopic current density $\mathbf{j}(\mathbf{r})$ connected to a coherent superposition of (a) a heavy-hole (HH) valence band state (bluish charge density) or of (b) a light-hole (LH) valence state and a conduction band state (reddish charge density). The lattice plane shown and \mathbf{k} are chosen such that the P orbitals of the HH state have there their maximum electron density.

In conclusion, nonequilibrium zone-edge TA phonons induce a relocation of valence electronic charge in cubic boron nitride, a behavior well beyond adiabatic phonon dynamics. A transfer of charge onto the boron and nitrogen atoms leads to a stronger charge localization and an increase of x-ray structure factors, in striking contrast to the usual Debye-Waller behavior. The pronounced coupling of zone-edge phonon excitations to electronic degrees of freedom is caused by local electric fields, the charge relocations serve to minimize the electrostatic energy of the excited crystal. Such behavior is relevant for a broad range of polar crystalline materials.

M. W. acknowledges support by the Deutsche Forschungsgemeinschaft (Grant No. WO 558/14-1). We thank Ceratonia GmbH for providing the samples for the impulsive stimulated Raman measurements.

*Present address: Physikalisch-Technische Bundesanstalt, 38116 Braunschweig, Germany.

†Present address: Research Neutron Source, Technical University of Munich, 85748 Garching, Germany.

‡reimann@mbi-berlin.de

§woerner@mbi-berlin.de

- [1] M. Born and K. Huang, *Dynamical Theory of Crystal Lattices* (Oxford University Press, London, 1954).
- [2] G. A. Garrett, A. G. Rojo, A. K. Sood, J. F. Whitaker, and R. Merlin, Vacuum squeezing of solids: Macroscopic quantum states driven by light pulses, *Science* **275**, 1638 (1997).
- [3] X. Hu and F. Nori, Phonon Squeezed States Generated by Second-Order Raman Scattering, *Phys. Rev. Lett.* **79**, 4605 (1997).

- [4] S. L. Johnson, P. Beaud, E. Vorobeva, C. J. Milne, É. D. Murray, S. Fahy, and G. Ingold, Directly Observing Squeezed Phonon States with Femtosecond x-Ray Diffraction, *Phys. Rev. Lett.* **102**, 175503 (2009).
- [5] D. M. Juraschek, M. Fechner, and N. A. Spaldin, Ultrafast Structure Switching through Nonlinear Phononics, *Phys. Rev. Lett.* **118**, 054101 (2017).
- [6] A. von Hoegen, R. Mankowsky, M. Fechner, M. Först, and A. Cavalleri, Probing the interatomic potential of solids with strong-field nonlinear phononics, *Nature (London)* **555**, 79 (2018).
- [7] W. Cochran, Theory of the lattice vibrations of germanium, *Proc. R. Soc. A* **253**, 260 (1959).
- [8] W. Cochran, Theory of the Lattice Vibrations of Germanium, *Phys. Rev. Lett.* **2**, 495 (1959).
- [9] W. Cochran and J. C. Phillips, Microscopic dielectric susceptibility of germanium, *Phys. Rev.* **134**, A1402 (1964).
- [10] J. H. Hannay, The Clausius-Mossotti equation: An alternative derivation, *Eur. J. Phys.* **4**, 141 (1983).
- [11] S. J. Fray, F. A. Johnson, and R. H. Jones, Lattice absorption bands in indium antimonide, *Proc. Phys. Soc.* **76**, 939 (1960).
- [12] M. Lax and E. Burstein, Infrared lattice absorption in ionic and homopolar crystals, *Phys. Rev.* **97**, 39 (1955).
- [13] G. Deinzer and D. Strauch, Two-phonon infrared absorption spectra of germanium and silicon calculated from first principles, *Phys. Rev. B* **69**, 045205 (2004).
- [14] R. Loudon, The Raman effect in crystals, *Adv. Phys.* **13**, 423 (1964).
- [15] F. Zamponi, P. Rothhardt, J. Stingl, M. Woerner, and T. Elsaesser, Ultrafast large-amplitude relocation of electronic charge in ionic crystals, *Proc. Natl. Acad. Sci. U.S.A.* **109**, 5207 (2012).
- [16] C. Hauf, A.-A. Hernandez Salvador, M. Holtz, M. Woerner, and T. Elsaesser, Soft-mode driven polarity reversal in ferroelectrics mapped by ultrafast x-ray diffraction, *Struct. Dyn.* **5**, 024501 (2018).
- [17] C. Hauf, A.-A. Hernandez Salvador, M. Holtz, M. Woerner, and T. Elsaesser, Phonon driven charge dynamics in polycrystalline acetylsalicylic acid mapped by ultrafast x-ray diffraction, *Struct. Dyn.* **6**, 014503 (2019).
- [18] B. E. Warren, *X-Ray Diffraction* (Dover, New York, 1969).
- [19] D. A. Evans, A. G. McGlynn, B. M. Towson, M. Gunn, D. Jones, T. E. Jenkins, R. Winter, and N. R. J. Poolton, Determination of the optical band-gap energy of cubic and hexagonal boron nitride using luminescence excitation spectroscopy, *J. Phys. Condens. Matter* **20**, 075233 (2008).
- [20] J. Weisshaupt, V. Juvé, M. Holtz, M. Woerner, and T. Elsaesser, Theoretical analysis of hard x-ray generation by nonperturbative interaction of ultrashort light pulses with a metal, *Struct. Dyn.* **2**, 024102 (2015).
- [21] M. Holtz, C. Hauf, J. Weisshaupt, A.-A. Hernandez Salvador, M. Woerner, and T. Elsaesser, Towards shot-noise limited diffraction experiments with table-top femtosecond hard x-ray sources, *Struct. Dyn.* **4**, 054304 (2017).
- [22] J. Weisshaupt, V. Juvé, M. Holtz, S. Ku, M. Woerner, T. Elsaesser, S. Ališauskas, A. Pugžlys, and A. Baltuška, High-brightness table-top hard X-ray source driven by sub-100-femtosecond mid-infrared pulses, *Nat. Photonics* **8**, 927 (2014).

- [23] See Supplemental Material at <http://link.aps.org/supplemental/10.1103/PhysRevLett.128.136402>, which contains additional details on data analysis, on the impulsive stimulated Raman scattering measurements, on the maximum entropy method, on the relation between Bragg reflections and valence electron density, and on the identification of the observed oscillations.
- [24] L. Dhar, J. A. Rogers, and K. A. Nelson, Time-Resolved Vibrational Spectroscopy in the Impulsive Limit, *Chem. Rev.* **94**, 157 (1994).
- [25] Y.-X. Yan, E. B. Gamble, Jr., and K. A. Nelson, Impulsive stimulated scattering: General importance in femtosecond laser pulse interactions with matter, and spectroscopic applications, *J. Chem. Phys.* **83**, 5391 (1985).
- [26] S. van Smaalen, L. Palatinus, and M. Schneider, The maximum-entropy method in superspace, *Acta Crystallogr.* **A59**, 459 (2003).
- [27] L. Palatinus and S. van Smaalen, The prior-derived F constraints in the maximum-entropy method, *Acta Crystallogr.* **A61**, 363 (2005).
- [28] M. Woerner, M. Holtz, V. Juvé, T. Elsaesser, and A. Borgschulte, Femtosecond X-ray diffraction maps field-driven charge dynamics in ionic crystals, *Faraday Discuss.* **171**, 373 (2014).
- [29] Y.-N. Xu and W. Y. Ching, Calculation of ground-state and optical properties of boron nitrides in the hexagonal, cubic, and wurtzite structures, *Phys. Rev. B* **44**, 7787 (1991).
- [30] N. Wahlberg, N. Bindzus, L. Bjerg, J. Becker, S. Christensen, A.-C. Dippel, M. R. V. Jørgensen, and B. B. Iversen, Powder x-ray diffraction electron density of cubic boron nitride, *J. Phys. Chem. C* **119**, 6164 (2015).
- [31] K. Karch and F. Bechstedt, Ab initio lattice dynamics of BN and AlN: Covalent versus ionic forces, *Phys. Rev. B* **56**, 7404 (1997).
- [32] J. L. Birman, Theory of infrared and Raman processes in crystals: Selection rules in diamond and zincblende, *Phys. Rev.* **131**, 1489 (1963).
- [33] There is a second two-phonon mechanism starting at $q = 0$, requiring a bandwidth corresponding to two TA phonon energies. This is larger than our $\Delta E_p = 50$ meV, making it irrelevant in our experiment.
- [34] K. Chen, B. Song, N. K. Ravichandran, Q. Zheng, X. Chen, H. Lee, H. Sun, S. Li, G. A. G. U. Gamage, F. Tian, Z. Ding, Q. Song, A. Rai, H. Wu, P. Koirala, A. J. Schmidt, K. Watanabe, B. Lv, Z. Ren, L. Shi, D. G. Cahill, T. Taniguchi, D. Broido, and G. Chen, Ultrahigh thermal conductivity in isotope-enriched cubic boron nitride, *Science* **367**, 555 (2020).
- [35] L. Bergman and R. J. Nemanich, Raman Spectroscopy for Characterization of Hard, Wide-Bandgap Semiconductors: Diamond, GaN, GaAlN, AlN, BN, *Annu. Rev. Mater. Sci.* **26**, 551 (1996).
- [36] V. G. Hadjiev, M. N. Iliev, B. Lv, Z. F. Ren, and C. W. Chu, Anomalous vibrational properties of cubic boron arsenide, *Phys. Rev. B* **89**, 024308 (2014).
- [37] F. Widulle, T. Ruf, O. Buresch, A. Debernardi, and M. Cardona, Raman Study of Isotope Effects and Phonon Eigenvectors in SiC, *Phys. Rev. Lett.* **82**, 3089 (1999).
- [38] J. L. A. Hemstreet and C. Y. Fong, Electronic band structure and optical properties of 3C-SiC, BP, and BN, *Phys. Rev. B* **6**, 1464 (1972).
- [39] J. A. Sanjurjo, E. López-Cruz, P. Vogl, and M. Cardona, Dependence on volume of the phonon frequencies and the ir effective charges of several III-V semiconductors, *Phys. Rev. B* **28**, 4579 (1983).